Water-assisted sonochemically-induced demethylenation of benzyl alcohol to phenol over a structurally stable cupric oxide catalyst

Teseer Bahry, Shang Jiang, Umesh Jonnalagadda, Wen Liu, Benoit Teychene, Francois Jerome, Samir Mushrif, Prince Nana Amaniampong

ARTICLE

Water-assisted Sonochemically-induced Demethylenation of Benzyl Alcohol to Phenol over a Structurally Stable Cupric Oxide Catalyst

Received 00th January 20xx,
Accepted 00th January 20xx

DOI: 10.1039/x0xx00000x

Teseer Bahry[a], Shang Jiang[b], Umesh Jonnalagadda[c], Wen Liu[c], Benoit Teychene[a], Francois Jerome[a], Samir H. Mushrif[b]*, Prince N. Amaniampong[a]*

Novel catalytic chemistry of demethylenation of benzyl alcohol to phenol is presented here using the synergy between an earth-abundant transition metal oxide (CuO) catalyst and high frequency ultrasound (HFUS). This chemistry is achieved in water and at room temperature. Using a combination of catalyst characterization, chemical and acoustic analysis, isotope labelling and density functional theory computations, we reveal the molecular reaction mechanism, involving benzaldehyde as an intermediate. Water is not just a benign solvation medium, but it directly participates in the chemistry by getting dissociated due to sonolysis. The adsorption of the OH from water on the catalyst surface inhibits its recombination. The surface adsorbed OH from water also activates the C-H bond in benzyl alcohol to form benzaldehyde and later incorporates itself into the phenyl ring to form phenol.

Introduction

When ultrasound interacts with a liquid, the liquid is locally subjected to depression, lowering the pressure below the vapor pressure of the sonicated liquid.[1, 2] This phenomenon generates cavitation bubbles composed of gas and vapors of liquid. Locally, high temperature and high pressure regions are generated when these microscopic cavitation bubbles implode.[3] These localised conditions can induce crucial chemical transformations.[3] The utilization of ultrasound (either high or low frequency) in chemistry application, often referred to as sonochemistry, has gained heightened attention in the last decade ever since the term was coined by Nappiras.[4] Sonochemistry, particularly high-frequency ultrasound (>100 kHz), has been widely used as an unconventional activation technique for material synthesis,[5, 6] environmental remediation[7] and food processing,[8] where acoustic cavitation-induced oxygenated radicals (e.g., •OH) act as initiators to trigger chemical reactions. Recently, the use of high-frequency ultrasound is undergoing a sort of renaissance as an alternative activation tool in synthetic chemistry and catalysis.[9-11] For instance, High frequency ultrasound (HFUS) was used as a combined strategy with metal ions to convert phenol and phenyl derivatives into polyphenols.[12] In a heterogeneous system, cavitation bubbles preferentially form on the particle surface *via* heterogeneous nucleation. In addition, these particles could serve as nuclei for the formation and growth of cavitation bubbles, a great means to enhance the formation of inertial cavitation. In contrast to a homogeneous system, the implosion of cavitation bubbles on solid surfaces generates high-speed jets of liquid directed toward the surface. This physical behavior could be a great way to selectively transfer sonochemically generated radicals onto the particle surface for better control of reaction selectivity. The technological potential

[a] *Institut de Chimie des Milieux et Matériaux de Poitiers, University of Poitiers, CNRS 1 rue Marcel Doré, 86073 Poitiers, France. E-mail : prince.nana.amaniampong@univ-poitiers.fr*
[b] *Department of Chemical and Materials Engineering, University of Alberta, 9211-116 St NW, Edmonton, Alberta T6G1H9, Canada*
E-mail : mushrif@ualberta.ca
[c] *School of Chemistry, Chemical Engineering and Biotechnology, Nanyang Technological University, 50 Nanyang Avenue, Singapore 639798*
† Footnotes relating to the title and/or authors should appear here.
Electronic Supplementary Information (ESI) available: [details of any supplementary information available should be included here]. See DOI: 10.1039/x0xx00000x

of high-frequency ultrasound, in synergy with catalysis, (sonocatalysis) in directly altering products' formations in synthetic chemistry has been sporadically demonstrated and documented in the literature.[5, 13] By choosing appropriate catalysts, unprecedented transformations can be achieved during sonocatalytic reactions. For instance, we recently demonstrated that, while CuO catalyst and HFUS are able to independently oxidize glucose to gluconic acid

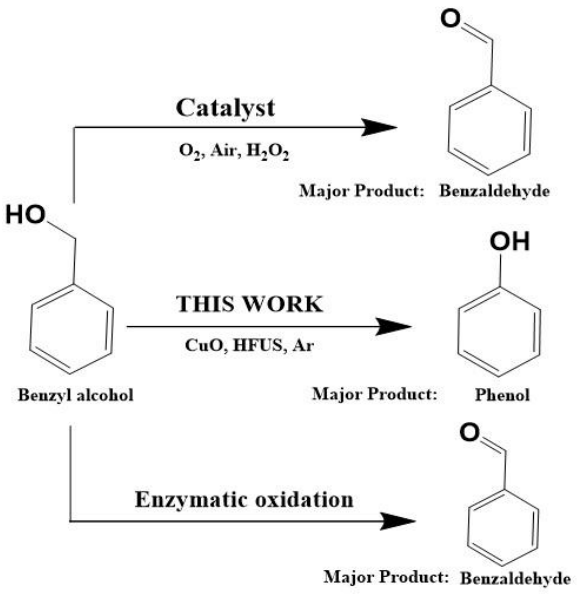

Scheme 1. Contribution of This Work to the State of the Art

under argon atmosphere, the combination of CuO with HFUS led to a complete selectivity switch, with glucuronic acid being formed as the major product.[5] Inspired by these works and in-line with our efforts in harnessing the synergistic potential of sonochemistry and catalysis for organic reactions, we revisited the widely studied benzyl alcohol oxidation reaction,[14-17] from a radically different perspective to gain first-hand insights into the mechanisms involved in its transformation to other aromatic products of industrial importance. Benzyl alcohol is one of the most widely studied substrates and model molecules in the literature.[14, 16, 18-20] Oxidative conversion of benzyl alcohol to benzaldehyde has been reported using a plethora of catalytic systems, including supported metal catalysts, with yields up to ~ 99% at elevated reaction temperatures, in the range of 100 °C.[14, 20] In the current state of the art, benzaldehyde has been shown to be the major product, along with trace amounts of benzoic acid in benzyl alcohol oxidation reactions. However, a tandem activation of benzyl alcohol in the presence of a relatively cheap metal oxide at mild conditions, driven demethylenation process into phenol is unprecedented. The development of alternative catalytic technologies capable of selectively demethylenating benzyl alcohol to phenol in a one-pot reaction is an important scientific challenge that is addressed in this work, as it will play a crucial role in finding alternative synthesis route to the industrially popular three-step cumene process where phenol is produced from benzene.[21] A process that suffers from several drawbacks such as high energy consumption, low yields (~ 5% based on the initial benzene quantity), and generation of acetone by-product.[22]

Herein, we demonstrate for the first time through combined experimental and theoretical investigations how the popular benzyl alcohol oxidation reaction (**Scheme 1**) can be systematically steered towards demethylenation, with up to 80 % selectivity towards phenol. This is achieved using the synergy between a sonochemically synthesized cupric oxide catalyst and ultrasonically generated *in-situ* •OH from water, at ambient conditions (25 °C), without any external oxidizing agent. This work would find application in the synthesis diverse hydroxyaromatic building blocks and generally offers potential for new, mild methods for efficient unmasking of phenol.

Materials and Methods

CuO catalyst synthesis. All chemical reagents were used without further purification. The synthesis protocol is adopted from our previous work.[23] Normally, a 80 mL of 0.25 M NaOH aqueous solution was added to 20 mL of 0.5 M $Cu(NO_3)_2$ aqueous solution, and a sky-blue suspension was obtained. This suspension was subsequently subjected to an ultrasonic irradiation at the desired high frequency, namely, 578 kHz, 864 kHz and 1140 kHz) and at a controlled temperature of 25 °C (standby power P_0 = 48 W, nominal electric power of the generator P_{elec} = 278 W at 578 kHz, P_{elec} = 305 W at 864 kHz and P_{elec} = 392 W at 1140 kHz), with an acoustic power in the water of $P_{acous.vol}$ = 0.10 $W{\cdot}mL^{-1}$ at 578 kHz, $P_{acous.vol}$ = 0.095 $W{\cdot}mL^{-1}$ at 864 kHz and $P_{acous.vol}$ = 0.089 $W{\cdot}mL^{-1}$ at 1140 kHz, determined by calorimetry.[24] A minichiller cooler (Huber) was used to control the reaction temperature at 25 °C. On completion of sonication at the desired time, the dark brown precipitates were washed thoroughly with distilled water and dried in an oven at 60 °C overnight.

Catalyst characterization. The as-prepared CuO morphology was studied by SEM and TEM. Prior to the SEM analysis, CuO sample in powder form was sprinkled onto carbon tape adhered to aluminum mounts. The SEM observations were then performed by using JSM-7900F Jeol microscope coupled with Energy-dispersive X-ray

spectrometer (EDS) Bruker 6/30. The images were made with the backscattered electron detector to highlight the Au particles on the support at 5kV. For the TEM analysis, the CuO sample in powder form was first mixed with ethanol, this solution was ultrasonicated to disperse the powder. A drop of this solution is then placed on a TEM Cu grid. This grid is placed in the microscope chamber under a secondary vacuum. The TEM images were recoreded using 2100 UHR 200kV Jeol (LaB_6) coupled with Energy-dispersive X-ray spectrometer (EDS) Jeol JED. The images were taken with conventional TEM (bright field) at 200kV. Surface area analysis was determined by nitrogen physisorption on a Micromeritics TrisStar apparatus. Briefly, CuO (80 mg) was measured by nitrogen adsorption/desorption isotherms at 77 K using a Micromeritics Tristar instrument after degassing the sample overnight at 140°C. The specific area was measured using the Brunauer-Emmett-Teller (BET) equation in the P/P_0 range 0.01-0.3.

Crystallographic analysis for the as-prepared catalysts was performed by means of XRD measurements in 2Θ mode on a Bruker AXS D8 diffractometer with CuKα (= 0.154056 Å) radiation at 40 kV and 20 mA. XPS analysis were carried out with a Kratos Axis Ultra DLD spectrometer using a monochromatic Al Kα source (1486.6 eV) operating at 150W (10mA, 15kV). Operating pressure of the spectrometer was 9×10^{-8} Pascal. The charge neutraliser system was operated for all samples who have an insulating feature.

High-resolution spectra were recorded using an analysis area of 300µm x 700 µm and 40 eV pass energy. This pass energy corresponds to Ag $3d_{5/2}$ FWHM of 0.55 eV. Data were acquired with 0.1 eV steps. The binding energy was calibrated using C1s binding energy fixed at 284.8 eV as an internal reference. The following binding energies regions were recorded: C1s, O1s, Cu2p, CuLMM. Atomic concentration ratios were calculated using sensitivity factors provided by the manufacturer. Peak fitting was achieved with Casa XPS software (version 2.3.24) applying Gaussian-Lorentzian profiles (Lorentzian 30%). Atomic force microscopy (AFM) was used to check the topography and surface roughness of the fresh CuO-864 catalyst and recovered CuO catalyst. Typically, 0.2 mg of CuO-864 kHz powder was dispersed in 1 mL of distilled water then a small drop of solution was deposited onto the upper surface of a muscovite mica and allowed to dry under air. Surface roughness was determined by using the SPM modular program Gwyddion. Dynamic light scattering (DLS) was used to determine the Particles Size distribution of the synthesized copper oxide particles, with the Standard Operating Procedure of the DLS instrument Zeta-sizer Nano ZS- Malvern.

Cavitation detection and analysis. To identify the broadband received cavitation energy from CuO-Nanoleave (NL), the Passive Cavitation Detector (PCD) data from each sine wave burst was processed by a power FFT to create a power spectral density (PSD) curve. For each burst, the integral of the PSD was computed and the power values along the broadband frequencies were summed across all the bursts to give the broadband received cavitation energy for a given experimental run. To calculate the cavitation intensity for a given burst, the PSD integral was normalized to the PSD integral of the water tank irradiated with ultrasound under the same conditions.[25-27]

Acoustic response analysis. To validate the cavitation threshold of the nanoleaves, a pulsed focused ultrasound setup was utilized as described in literature.[27-29] In brief, an acoustically transparent flow chamber was constructed, comprising of a 1 mm channel in a 2 wt% agarose (Vivantis, #PC0701). A CuO nanoleaf suspension (1 mg/mL, 10 mL) was then perfused through the channel using a syringe driver set to 500 µL/min. A control solution was distilled water without catalyst was used as a control to validate the cavitation response of degassed water. The focused ultrasound transducer (centre frequency at 1.1 MHz, H102, Sonic Concepts) was aligned to the centre of the chamber to irradiate the solution at 20 seconds intervals (20 µsec pulse length, 10 Hz PRF, 1.8—19 MPa Peak Negative Pressure). The PCD signal was unfiltered, but all other experiments utilized an analogue 2.5 MHz high-pass filter (Allen Avionics F5286-2P50-B) before amplification through a broadband amplifier (5x, SRS SR445A). This processed signal was captured on the oscilloscope (National Instruments, USA PCI-5122) and saved for later processing as described previously.[26, 28] The cavitation data were analysed as described above using a threshold intensity of 10 dB and the probability of cavitation at each pressure level was quantified as the pulses greater than the cavitation threshold over the total number of pulses ($p(P) = \frac{\mathrm{P_{pulses,cavitation}}}{\mathrm{P_{pulses,total}}}$).

The cavitation threshold was calculated from the cavitation potential curve using a sigmoid fit ($p(P) = \frac{1}{1+e^{-k(P-P_{50})}}$), where p(P) is the cavitation probability for a given peak negative pressure, P, P_{50} is the pressure at which cavitation occurs 50% of the time and k is the intercept coefficient.

Hydrogen Peroxide (H_2O_2) quantification. The H_2O_2 concentration in the solution was measured using a UV visible spectrophotometer (ThermoFisher Evolution 60S).

Principle. H_2O_2 reacts with TiO_2^+ to form a yellow-orange complex Ti(IV)-H_2O_2. The absorption spectrum of this complex shows a maximum absorption wavelength at 412 nm.

Calibration curve. $TiOSO_4$ solution 0.02 M in H_2SO_4 0.5M. Typically, 0.552 g of titanium oxysulfate ($TiOSO_4$) are dissolved in water and then 2.8 mL of H_2SO_4 (18 M) are added. The solution was then diluted with water to a final volume of 100 mL.

Standard solutions of H_2O_2. The hydrogen peroxide solutions were prepared from a commercial H_2O_2 solution (35%w) at concentrations between 0 and 0.005 M. For the calibration curve, the analysis was performed by mixing the same volume of the $TiOSO_4$ solution and hydrogen peroxide solution (0.5 mL) (in order to obtain a dilution by 2 of the H_2O_2 solution). The absorbance was measured at 412 nm.

Benzyl alcohol Oxidation. Oxidation of Benzyl alcohol was carried out in a 250 mL high-frequency ultrasonic reactor (Meinhardt Ultrasonics Multifrequency Ultrasound reactor with a functional generator). Typically, 5 mM of benzyl alcohol in 100 mL of distilled water and 10% w of copper oxide CuO catalyst (equivalent to 5.4 mg) were introduced into the ultrasound cup-horn reactor. The solution was bubbled with Argon at a flow rate 20 mL min^{-1} and subjected to high-frequency ultrasound irradiation at a controlled temperature of 25 °C and a frequency of 578 kHz (standby power P_0 = 48 W, nominal electric power of the generator P_{elec} = 278 W), with an acoustic power in the water of $P_{acous.vol}$ = 0.11 W·mL^{-1} determined by calorimetry technique.

The oxidation of benzyl alcohol into phenol is described using three parameters: Benzyl alcohol conversion, phenol yield, and selectivity for phenol. These are calculated according to the following equations:

$$Benzyl\ alcohol\ conversion\ (\%) = \frac{Concentration\ of\ benzyl\ alcohol\ reacted\ (mM)}{Initial\ concentration\ of\ benzyl\ alcohol\ (mM)}$$

$$Products\ yield\ (\%) = \frac{Concentration\ of the\ \ product\ formed\ in\ the\ solution\ (mM)}{Theoretical\ \ concentration\ of\ the\ product\ (mM)}$$

Product analysis. The products were analyzed using a Thermo Scientific™ Vanquish™ Core HPLC system equipped with a quaternary pump system a variable wavelength UV-visible detector, an autosampler Split Sampler CT, and an Extend-C18 Agilent column (4.6 mm × 250 mm). Benzyl alcohol, Benzaldehyde and Phenol were quantified using a mixture of acetonitrile/water (55:45) as a mobile phase (1 mL.min^{-1}) at 25 °C. Hydroxy-benzyl alcohol (*ortho*-hydroxy-benzyl alcohol, *meta*-hydroxy-benzyl alcohol and *para*-hydroxy-benzyl alcohol), hydroxy- Benzaldehyde (*meta*-hydroxy-Benzaldehyde and *para*-hydroxy- Benzaldehyde), hydroquinone, catechol and *p*-benzoquinone were quantified using a mixture of acetonitrile/water (25:75) as a mobile phase (0.5 mL.min^{-1}) at 25° C.

LC-MS analysis. The HPLC–MS system consisted of UHPLC Ultimate 3000 by thermoscientific coupled with high resolution mass spectrometer (HRMS) IMPACT HD by BRUKER equipped with an electrospray ionizer source (MS; ESI). Reversed-phase HPLC separation was carried out using a Thermo Scientific™ Hypersil GOLD™ C18 column (2.1 mm × 50 mm). The mass spectrometer was operated in negative ion mode with capillary voltage, 3.0 kV, dry gas: N_2, the dry gas temperature was 200 °C and the flow was 4 L.min^{-1}. Phenol was analysed as follow: the mobile phase components were 0.1% formic acid in acetonitrile (A) and 100 % water (B). The mobile phase gradient was: 0–30 min, 5%-95% A; 30– 32 min, 95%–5% A; 32–34 min, 95%–95% A. The injection volume was 15 µL and the column temperature was 30 °C. The flow rate of the mobile phase was 0.4 mL.min^{-1}. Hydroxy-benzyl alcohol (ortho-hydroxy-benzyl alcohol, meta-hydroxy-benzyl alcohol and para-hydroxy-benzyl alcohol), hydroxy- Benzaldehyde (meta-hydroxy- Benzaldehyde and para-hydroxy- Benzaldehyde), hydroquinone, catechol and *p*-benzoquinone were analysed using the extend-C18 Agilent column (4.6 mm × 250 mm) and a mixture of acetonitrile/water (55:45) as a mobile phase (1 mL.min^{-1}). The injection volume was 15 µL and the column temperature was 25 °C.

Computational methods. All DFT calculations were done using the Vienna ab initio simulation program (VASP) [30-33]. The plane-wave basis set with the cut-off kinetic energy of 450 eV, the projector-augmented wave (PAW) [34, 35] and the Perdew–Burke–Ernzerhof (PBE) functional[36] with the vdW-DFT[37, 38] enabled were utilized for these simulations. According to *Bhola et. al.* [39] and *Trinh et. al.*[40], the appropriate surface-specific U value should be used to predict the surface reactions, pathways, and energetics, instead of U value optimized for bulk properties. Hence, GGA+U method with the

Hubbard U correction of 4.0 eV was used as it could successfully capture the surface O1s core level binding energy and experimental surface adsorption enthalpy on CuO (111) surface. In this study, CuO was modelled as periodic four-layer slabs and a 15 Å vacuum thickness above the top layer was used to prevent the interaction between repeated periodic unit cells. The top layer and the adsorbates were allowed to fully relax while the bottom two layers were fixed at the optimized bulk lattice parameters to reduce the computational cost without influencing the accuracy of simulations. The convergence criteria for total energy and interatomic forces were set to 10^{-6} eV per unit cell and 0.01 eV/A, respectively. All the calculations were performed with spin polarization as the antiferromagnetic ground state of CuO[40]. The 4 × 3 × 1 Monkhorst–Pack grid was used to sample the Brillouin zone, and the tetrahedron method with Blöchl corrections was employed for all calculations. Transition states were reached using the Nudged Elastic Band (NEB) method[41-44] and confirmed with the vibrational frequency calculations with only one imaginary frequency. To obtain the free energies of the process, the entropy, zero-point energy and enthalpy correction were computed from statistical thermodynamics for all adsorbed structures, while those values for gas-phase molecules were taken from the standard thermodynamics NIST-JANAF table[39, 45, 46].

Results and Discussions

CuO catalyst preparation and characterization. Inspired by the inexpensive but catalytic attributes of CuO, we prepared a series of copper oxide catalysts with a leaf-like morphology at different ultrasound frequencies (578, 864 and 1140 kHz, wherein referred to as CuO-578, CuO-864 and CuO-1140) following a sonochemical protocol developed in our group.[5] Detailed preparation protocol of the synthesized catalysts is described in the methods section. The fresh CuO-864 nanostructured catalyst (chosen for all the experimental investigations based on their structural uniformity and polydispersity after synthesis) was characterized by XRD, SEM, TEM, AFM and XPS techniques (**Figure 1**). XRD patterns (**Figure 1a**) with major peaks centered at 2Θ = 35.5° and 38.8° are indexed as CuO [-1 1 1] and CuO [1 1 1], respectively, which are characteristics of the pure monoclinic CuO crystallites phase. SEM **(Figure 1b)**, TEM **(Figure 1c)** and AFM investigations (**Figure 1d)** altogether confirmed the leaf-like morphology of the as-synthesized CuO. The AFM analysis further

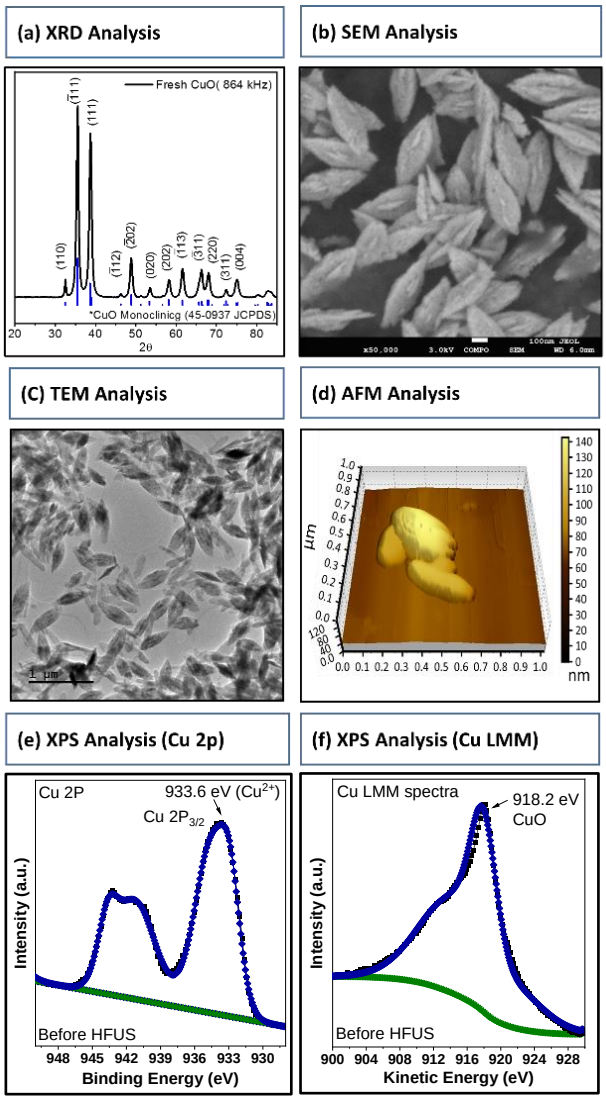

Figure 1. (a) XRD analysis (b) SEM analysis (c) TEM analysis (d) AFM analysis (e) XPS Cu2p analysis (f) XPS Cu LMM analysis, of as-prepared CuO catalyst.

revealed a CuO particle surface roughness and height of 0.85 x 10^{-3} ± 0.35 µm and ~ 64 nm, respectively. The XPS analysis of the as-prepared CuO nanoleaves confirmed the formation of Cu^{2+} with binding energy centered at 933.6 eV, which is attributed to the core level of Cu 2p $^{3/2}$ (**Figure 1e**). Additional peaks occurring at 941 and 943 eV are due to the shakeup satellite peaks. Analysis of the Cu LMM spectra revealed a peak with kinetic energy centered at 918.2 eV (**Figure 1f**), characteristic of CuO nano-structured material, and significantly ruling out the possibility of the existence of a Cu_2O phase.[40] Dynamic light scattering (DLS) analyses were also investigated to confirm their size uniformity of the leaf-like CuO catalysts synthesized (**Table S1**) under ultrasound irradiation.

Sonocatalytic demethylenation of benzyl alcohol to phenol. Prior to catalytic reactions, using an external H_2O_2 calibration (**Figure S1**), we investigated the *in-situ* production of hydrogen peroxide (H_2O_2) under an argon atmosphere during the irradiation of water at high-frequency ultrasound (578, 864 and 1140 kHz) using an external H_2O_2 calibration (**Figure S2**). During sonochemical irradiation of water under argon atmosphere, vapors of water trapped in the cavitation bubbles can be pyrolyzed to yield •OH and •H radicals. These radical species can recombine to form H_2O_2 and H_2, respectively.[47] Hence, pure water was sonicated at a controlled temperature of 25 °C, and the formation of H_2O_2 was monitored using a standardized spectro-photochemical method. After 90 min of irradiation, ~ 1.4 mmol.L^{-1}, ~ 1.1 mmol.L^{-1} and 1.0 mmol.L^{-1} of H_2O_2 concentrations were observed for 578, 864 and 1140 kHz ultrasonic frequencies, respectively, suggesting the successful *in-situ* formation of H_2O_2 in neat water

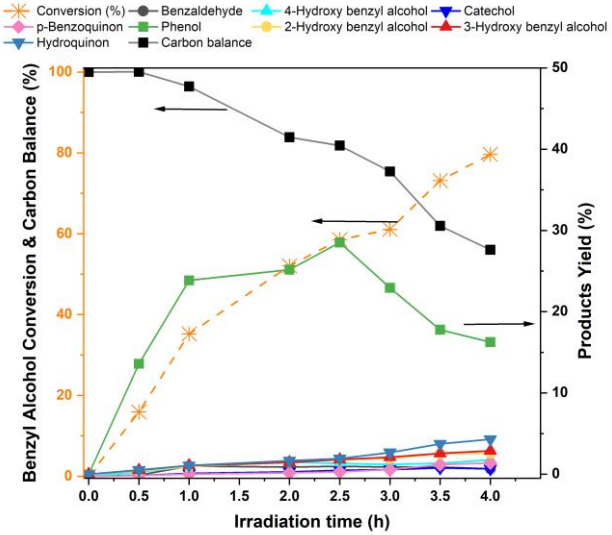

Figure 2. Conversion of benzyl alcohol and products yields in the ultrasound reactor, as a function of time. Reaction conditions: 5 mmol.L^{-1} Benzyl alcohol, 5.4 mg CuO, 578 kHz, 0.11 W/mL, 25 °C

(**Figure S2**). Based on the concentrations of H_2O_2 obtained, the ultrasound frequency of 578 kHz was selected for all other sono (catalytic) reactions, unless otherwise stated. Catalytic performance tests, with benzyl alcohol as the reactant were conducted in the high frequency (578 kHz) ultrasound reactor in the presence of argon bubbling (20 mL.min^{-1}) at a controlled reaction temperature of 25 °C. Without adding the catalyst, less than 15 % yield of phenol was observed at a benzyl alcohol conversion of 33 %, within 1.5 h of reaction time. Extending irradiation time negatively impacted phenol formation (< 10 % yield) (**Figure S4a**) owing the uncontrolled over-oxidation of phenol to other hydroxylated products. Next, reactions where performed in the presence of CuO-864 nanoleaf catalyst (**Figure 2**). Phenol yields were determined at a reaction irradiation time span of 0.5-4 h. A rapid increase in the conversion of benzyl alcohol was observed from 16 % to 80 %, from 0.5 h to 4 h of reaction time. However, the yield of phenol increased gradually from 13 % to 30 %, from 0.5 h to 2.5 h of irradiation time, then decreased steadily from 30 % to 15 %. The yield of phenol did not change (15 %) even after extended irradiation time of 6 h at complete conversion of benzyl alcohol. Phenol once formed *in-situ* can be a potent hydroxyl radical scavenger and reacts rapidly with the •OH thereby resulting in further transformation of phenol to hydroxylated phenolic products. This explains the drop in yield of phenol after 2.5 h of irradiation time. The initial increase in the yield of phenol demonstrates the synergy between the CuO catalyst and the ultrasound irradiation in driving the demethylenation of benzyl alcohol and steering it away from an uncontrolled oxidation reaction. Detailed analysis of the reaction products revealed the formation of benzaldehyde, hydroxy-benzyl alcohol (*ortho*-hydroxy-benzyl alcohol, *meta*-hydroxy-benzyl alcohol and *para*-hydroxy-benzyl alcohol), hydroxy-benzaldehyde (*meta*-hydroxy-benzaldehyde and *para*-hydroxy-benzaldehyde), hydroquinone, catechol and benzoquinone (with a total yield of 3 % to 14 %, after 0.5 h to 4 h of reaction irradiation time). The identification and quantification of these products provided clues to the reaction mechanism of the formation of phenol and its subsequent reactions (after reaching a maximum at 2.5 h) with the increase in irradiation time. To confirm the structural integrity and stability of the CuO calatyst, characterization of the spent catalyst (described later in the manuscript) and inductively coupled plasma with optical emission spectrometer (ICP-OES) analysis were performed. ICP-OES results of the crude reaction product (after 4 h of reaction time) obtained after filtration revealed slight Cu leaching of 9 ppm. Considering this level of copper leaching, we further investigated the stability of the stability in a recycling experiment by performing sonocatalytic reactions over four-cycles (**Figure S4b**). All reactions were performed at an iso-conversion of 22 %. The selectivity towards phenol was observed to be ~ 85 % after the 1st and 2nd cycles but dropped slightly to ~ 79 % after the 3rd and 4th cycles. The yield towards benzaldehyde was observed to increase after the 3rd and 4th cycles to ~10 %, from ~ 5 % after the 1st and 2nd cycles.

Acoustic Response, Cavitation Behavior and radicals interactions with CuO nanoleaves. It has been established that the presence of solid particles in irradiating solutions could enhance the formation of cavitation bubbles *via* the principle of heterogeneous cavitation. To probe into this phenomenon, we next assessed the; (1) acoustic response of the CuO-864 nanoleaves catalysts and their propensity to nucleate cavitation through a range of peak negative pressure amplitudes, in line with the principle of heterogeneous cavitation, and (2) transfer of radicals produced inside the cavitation bubble onto a solid catalyst surface during cavitation bubbles implosion, by investigating the *in-situ* formation of H_2O_2 in the presence of CuO-864 solid catalyst (**Figures. 3**). Catalysts prepared at different ultrasound frequencies were also investigated (**Figure S2**). CuO-864 catalyst exhibited a cavitation threshold at 7.59 ± 0.57 MPa peak negative pressure. Comparably, neat water cavitated less efficiently under this pressure regime, indicating that CuO-864 nanoleaves enabled gas nucleation for an enhanced cavitation response at reduced pressure amplitude (**Figure 3a**). The increase cavitation response exhibited by the CuO nanoleaves is likely due to surface roughness (confirmed by AFM analysis) which is able to stabilize gas bubbles.[48-50] In addition to the acoustic response profile, we validated the frequency content above and below the cavitation thresholds for our synthesized CuO-864 nanoleaves catalyst (**Figure 3b**). Here, we observed that prominent broadband noise at and above the cavitation threshold, which is indicative of inertial cavitation.[51-53] From this, we confirm that the presence of CuO nanoleaves during sonolysis not only resulted in enhanced acoustic response, but also promoted inertial cavitation, which is of primary importance to radical generation and oxidative processes in macroscopically ambient conditions. The time for which the CuO catalysts sustain their cavitation response is crucial, as it's an indication of the duration over which the CuO catalysts remain fully functional during continuous irradiation. To this end, in addition to the initial intensity of inertial cavitation (**Figure 3b**), we investigated the duration of cavitation both in the presence of the CuO catalyst and neat water over 10 minutes of irradiation at a 33 % duty cycle (**Figure 3c**) to probe into the ability of CuO catalyst in sustaining localized inertial cavitation. Over the 10 min irradiation, we observed a consistent cavitation response in the presence of CuO nanoleaves. Whereas a sporadic acoustic intensity was observed in the presence of neat water. These results indicate that the CuO nanoleaves function as a nucleation site for cavitation to occur, thereby continuously sustaining inertial cavitation formation. In neat water, the stochastic and random nature of cavitation events leads to a rather sporadic acoustic intensity. Next, the rate of *in-situ* H_2O_2 formation was investigated in the presence of CuO catalyst under irradiation. After 90 min of irradiation in the presence of CuO solid catalysts, the concentrations of H_2O_2 were observed to be ~ 0.3 mmol. L^{-1} (production rate of 5.8 x 10^{-8} mol. L^{-1}. s^{-1}) and 0.25 mmol. L^{-1} (production rate of 5 x 10^{-8} mol. L^{-1}. s^{-1}) over CuO-578 and CuO-1140 catalysts, respectively (Figure S2). Whereas H_2O_2 concentration observed over CuO-864 catalyst was only ~ 0.1 mmol. L^{-1} (production rate of 1.6 x 10^{-8} mol. L^{-1}. s^{-1}) (Figure 3d), which is 93 % lower than that observed (1.4 mmol. L^{-1}, production rate of 24.8 x 10^{-8} mol. L^{-1}. s^{-1}) (Figure 3d) in pure water, in the absence of CuO. This suggests that radicals formed during the ultrasonic irradiation of water interact with the surface of the CuO solid catalyst. The interaction with the catalyst significantly limits the diffusion of OH radicals into the bulk phase and their subsequent recombination to form H_2O_2. The recovered CuO-864 catalyst after ultrasound irradiation was dried overnight in an oven at 60 °C without any further post-treatment and again introduced into the ultrasound reactor to re-evaluate its impact on the production of H_2O_2. The observed rate of H_2O_2 formation (**Figure 3d**) was strikingly similar to the fresh CuO-864 catalyst, suggesting that high-frequency ultrasound irradiation did not impact the structural integrity of the CuO catalyst. To further confirm this, x-ray diffraction (XRD), X-ray photoelectron spectroscopy (XPS) and scanning electron microscopic (SEM) analyses of the fresh and recycled CuO (after ultrasonic irradiation) were also performed (**Figure S3**). Furthermore, to confirm that CuO particles indeed interact with the sonolytically generated radicals, a hot filtration test was performed after 60 min of irradiation in the presence of CuO catalyst, where the CuO catalyst was filtered out of the solution and irradiation was initiated again on the blank water (**Figure 3e**). An increase in the rate of H_2O_2 formation was observed, reaching 0.45 mmol. L^{-1} (production rate of 10.5 x 10^{-8} mol. L^{-1}. s^{-1}) (from 0.1 mmol. L^{-1}, production rate of 1.6 x 10^{-8} mol. L^{-1}. s^{-1} in the presence of CuO). This confirms the interaction of the CuO solid catalyst with OH radicals generated during the irradiation and the suppression OH recombination to H_2O_2 by the catalyst. Although the production rate of H_2O_2 increased significantly once the CuO materials was recovered, the production rate was lower than that of the neat water after 1 h irradiation time. We have repeated these reactions again and they are reproducible. We performed an ICP

analysis on the filtrate solution after the CuO removal and copper leach of 0.0015pmm, this amount of copper in the homogeneous solution might not be so innocent in the decomposition of H_2O_2 once formed *in situ* during sonolysis. We are indeed investigating the roles of homogeneous metal catalysts on H_2O_2 formation during ultrasound irradiation. However, this reaction is currently beyond the scope of this current work (paper). Altogether, these results demonstrated the potential of CuO catalyst in steering the selective formation of phenol from benzyl alcohol, while serving as a nucleation agent and enhancing catalyst-radical interaction intimacy without compromising its stability and structural integrity.

To identify the role of the radicals generated during irradiation in the overall reaction, we further conducted a series of inhibition and isotope-labelling experiments. First, *tert*-Butanol (TBA) was chosen as radical scavenger owing to its ability to effectively scavenge •OH.[54] As expected, the addition of TBA led to a total inhibition of phenol formation even after 4 h of reaction irradiation time, indicating the efficient scavenging of •OH radicals responsible for the inhibition of the formation of phenol. The quenching results reveal that •OH radicals contribute to the selective demethylenation of benzyl alcohol to phenol. Next, deuterated water (D_2O) was selected as a solvent to confirm the insertion of OH originating from water sonolysis and not from the alcohol group in benzyl alcohol into the product phenol. High-resolution mass spectrometric (HR-MS) analysis of the crude reaction product revealed the appearance of a peak at m/z = 94.0412 g/mol, confirming the incorporation of •OD in phenol (**Figure S5**).

The temperature of the ultrasound reactor was next increased from 25 °C to 60 °C to investigate the impact of bulk liquid temperature on the sonocatalytic reaction. At 60 °C, phenol selectivity was not significantly impacted, however, the rate of benzyl alcohol conversion was slower (**Figure S6**) compared to the reactions at 25 °C (**Figure 2**). The increase in the bulk temperature of the solution lowers the threshold of cavitation bubble production, increases vapor pressure, and decreases surface tension, which can concomitantly weaken bubble collapse intensity. This negatively impacts the rate of formation of oxygenated radicals during bubble implosions. As expected, a maximum phenol yield of ~ 18 % at a conversion of 52 % within the reaction irradiation time of 6 h, was observed at 60 °C, as compared to 30 % phenol yield at ~ 60 % conversion within 1.5 h irradiation time, at 25 °C. These results are in agreement with the sonoluminescence study reported by Pickworth et al.,[55] and Didenko et al. [56] where sonoluminescence intensities (physical indication of hot-spot temperature created during cavity implosion) were found to decrease with the increase in temperature. To explore other reaction parameters, we investigated the effect of substrate concentrations (**Figure S7**) and catalyst loading (**Figure S8**). Detailed results are shown in the supporting information.

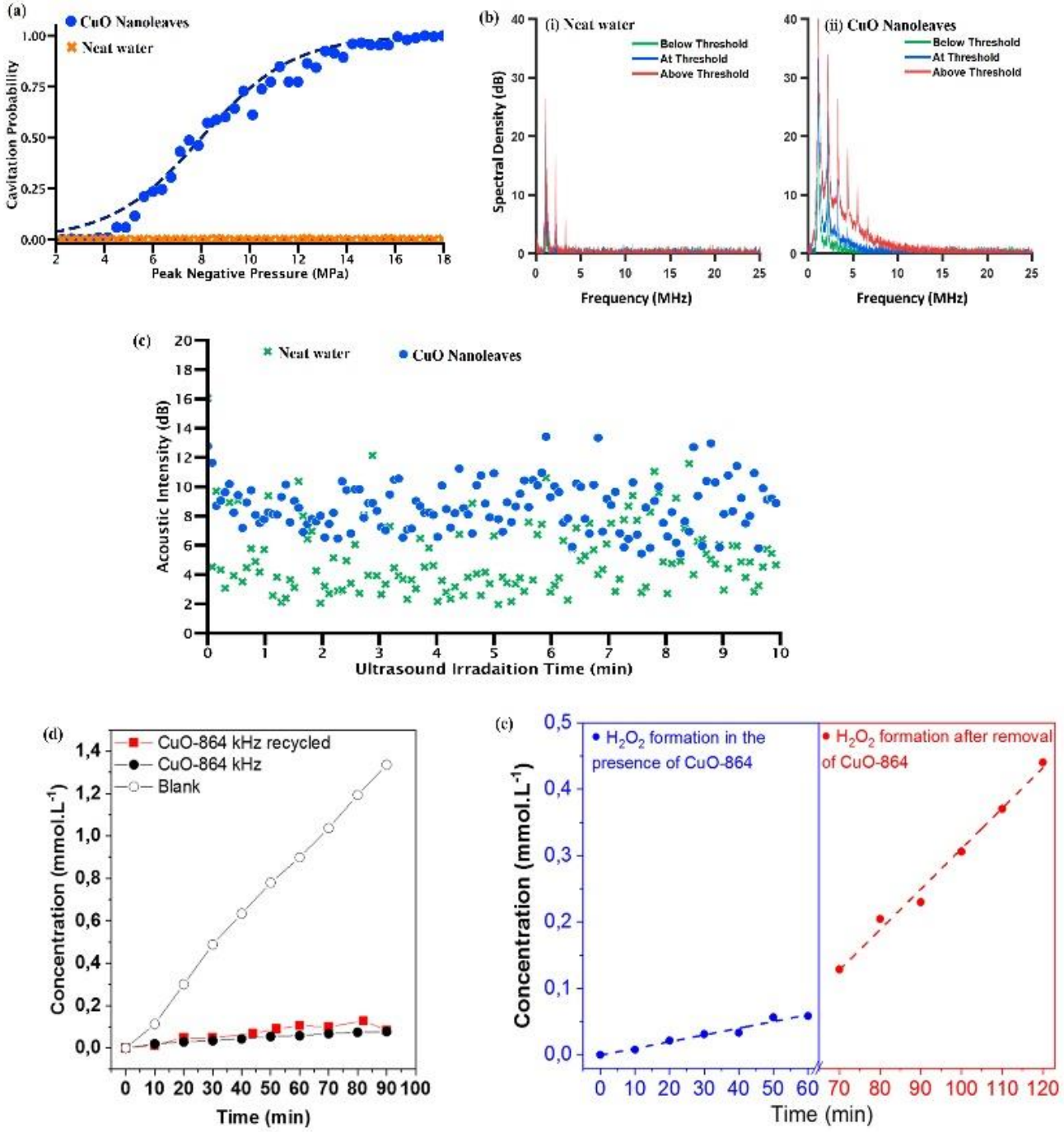

Figure 3. (a) Cavitation potential of CuO nanoleaves and neat water at various acoustic pressures. (b) Power spectral density was further analyzed to validate the quality of noise. The power spectral density curve expressed greater evidence of broadband cavitation in the presence of CuO Nanoleaves (c) visualization of acoustic response of CuO particles and neat water by assessing the acoustic cavitation intensity *vs* time (d) *In-situ* formation of H_2O_2 in the presence and absence of CuO catalyst (e) *In-situ* formation of H_2O_2 in the presence of CuO-864 catalyst (blue code), in-situ formation of H_2O_2 during hot filtration test (red code). 578 kHz, 0.11 W.mL^{-1}, 25 °C.

Experimental insights into the reaction mechanism. To get insights into the reaction mechanism, first, benzaldehyde was tested as a reactant (Table S2, entry 1-4). In this case too, phenol was observed as the major product (~ 11 %) after 30 min, at a conversion of 23 %. The yield increased steadily to 23 % after 2.5 h, at a conversion of 66 %, along with trace amounts of *para*-hydroxy-benzaldehyde (< 1%). These results suggest that benzaldehyde is an intermediate in the formation of phenol from benzyl alcohol. No benzoic acid was detected in reaction products, possibly suggesting that the formation of phenol does not go through benzoic acid decarboxylation.

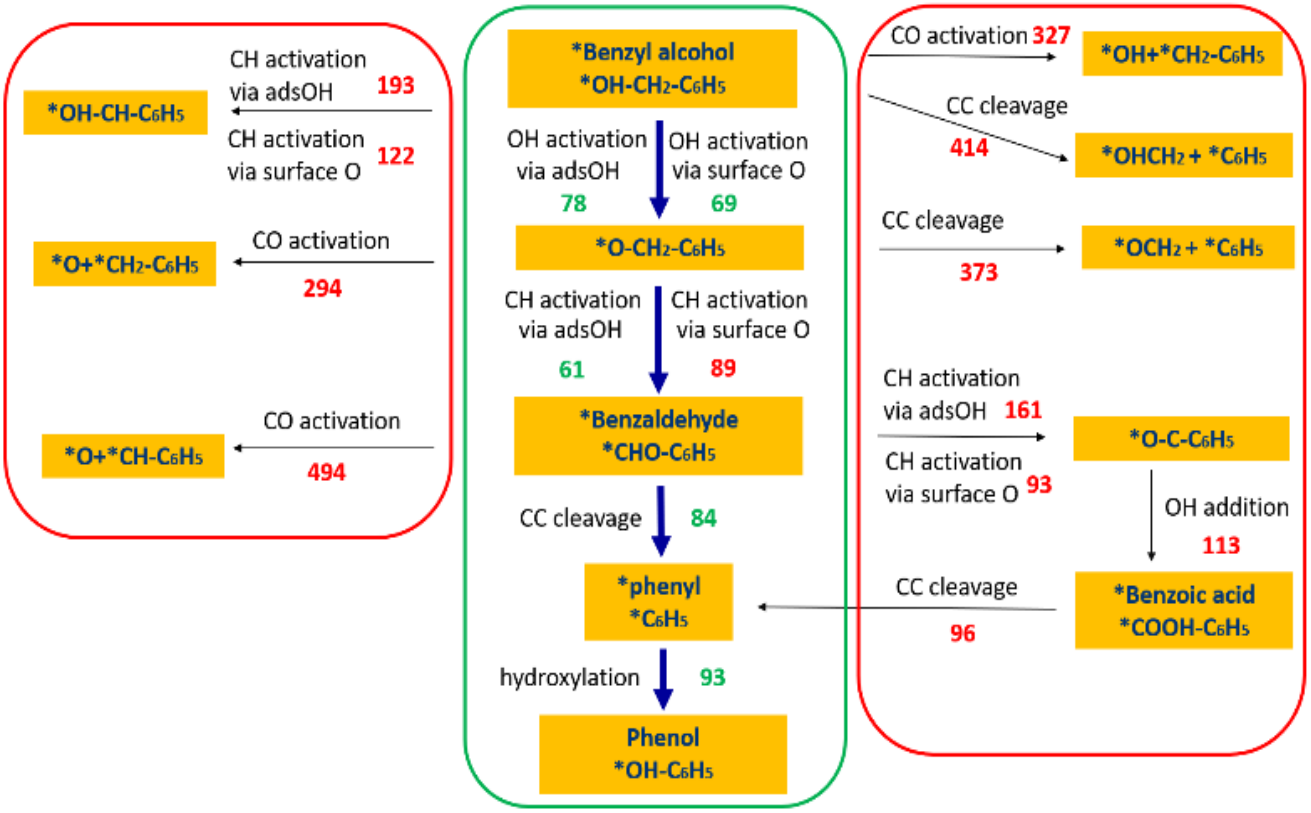

Figure 4. Mechanisms and energy profiles of the conversion of benzyl alcohol to phenol on CuO (111). Activation free energy barriers (E_a) in kJ/mol are shown. Green values are activation barriers for the kinetically favourable reaction steps and red values indicate the activation barriers of reaction steps which are less favourable. Bold blue arrows indicate the preferred reaction pathway.

However, when benzoic acid was used as a substrate, phenol (24 % yield at 76 % conversion within 5 h irradiation time) was produced, as confirmed by DFT calculations (discussed later). To assess the possibility of phenol formation *via para*-hydroxyl benzyl alcohol as an intermediate, *para*-hydroxyl benzyl alcohol was used as a reactant in the sonocatalytic reaction (Table S2, entry 5-8). Hydroquinone was observed as the major product with a yield of ~ 8 % at a conversion of ~ 26 % within 1 h of reaction irradiation (Table S2, entry 5), which further increased to 15 % yield at a conversion of 72 %, after 3 h reaction irradiation. Noteworthy, benzoquinone and *para*-hydroxyl benzaldehyde were formed alongside hydroquinone with yields of ~ 4 % and ~ 2 %, respectively. It is also interesting to state that, no phenol was formed when hydroxyl benzyl alcohol was used as substrate. This confirms that, (i) benzaldehyde is an intermediate species in the formation of phenol and (ii) the hydroxylation of benzyl alcohol is not a key step to form phenol and also that the presence of an additional hydroxyl group in benzyl alcohol (*para*-hydroxyl benzyl alcohol) does not alter the reaction pathway and the activation of the alcohol group.

To evaluate the role of high-frequency ultrasound irradiation in the overall reaction, the reaction of benzyl alcohol catalyzed by CuO was performed under silent conditions (that is, in the absence of ultrasound). Under silent conditions at 25 °C and 100 °C in argon flow, no benzyl alcohol conversion and product formation were observed (Table S3 entry 1 and 2). However, reactions performed in the presence of $H_2O_{2(aq)}$ under silent conditions at 62 °C resulted in the formation of a trace amount of phenol (1% yield) at a benzyl alcohol conversion of 9 % within 1 h of reaction time (Table S3, entry 3). Upon increasing the reaction time from 2h to 6h, the conversion of benzyl alcohol increased to ~ 35 % at 2 h and remained constant even up to 6 h reaction time. The phenol yield behaved similarly; phenol yield of ~ 13 % at 2h, which then plateaued from 3 h to 6 h. The depletion of H_2O_2 under silent conditions during the course of the reaction explains the plateau in conversion and yield after 2h reaction time. These results further reinforce the importance of high-frequency ultrasound in the continuous generation of *in-situ* OH radicals from water and its synergy with CuO catalysts, which is crucial for the demethylenation catalytic reaction.

Computational Investigations into benzyl alcohol conversion to phenol on CuO (111). Density functional theory (DFT) calculations were performed to (1) elucidate the detailed reaction mechanism and compute activation free energy barriers and reaction free energies of the catalytic conversion of benzyl alcohol to phenol; (2) investigate the dissociation of water on the catalyst surface and the role of water and H_2O_2 in the reaction; and (3) confirm the postulated reaction mechanism of the catalytic conversion of benzaldehyde and *para*-hydroxy-benzyl alcohol; in line with the experiments performed in the presence of H_2O_2 under silent conditions. CuO (111) was chosen for the computational investigation as it is the thermodynamically most stable facet of the pure monoclinic CuO and agrees with the experimental XRD data shown in **Figure 1a**. **Figure 4** shows the pathways for the conversion of benzyl alcohol to phenol (catalyzed by lattice oxygen and by •OH generated due to ultrasound-induced water dissociation), including the O-H, C-H, and C-C activation and the corresponding free energy activation barriers for each elementary reaction step. The most favourable pathway is highlighted, and its free energy profile along each elementary reaction step is shown in **Figure 5**. All reported free energy barriers and reaction free energies are computed at 25 °C (the entropy, zero-point energy and enthalpy correction were all considered).

Benzyl alcohol to phenol reaction mechanism. As experimental results suggest, the OH group from water or H_2O_2 plays a role in the conversion of benzyl alcohol to phenol. OH groups on CuO (111) surface have been previously shown to lower the barrier for C-H activation in glycerol significantly. [45] Thus, surface adsorbed OH groups assisted pathways are also evaluated, as shown in **Figure 4**. On a clean CuO (111) surface, benzyl alcohol is activated via its alcohol group, and the activation free energy barriers for O-H cleavage are 78 and 69 kJ/mol via the surface adsorbed OH group and surface lattice oxygen, respectively. Alternate first activation pathways such as direct C-C cleavage, C-H activation (via surface oxygen and surface adsorbed OH group) or C-O activation have significantly higher activation barriers of 414, 122, 193 and 327 kJ/mol, respectively, as can be seen in **Figure 4.** O-H activation is slightly preferred via the surface lattice oxygen, both kinetically and thermodynamically. As the OH of the benzyl alcohol group is activated, a bridge configuration is formed through the two surface copper atoms and oxygen in the intermediate structure I1 (**Figures 5**

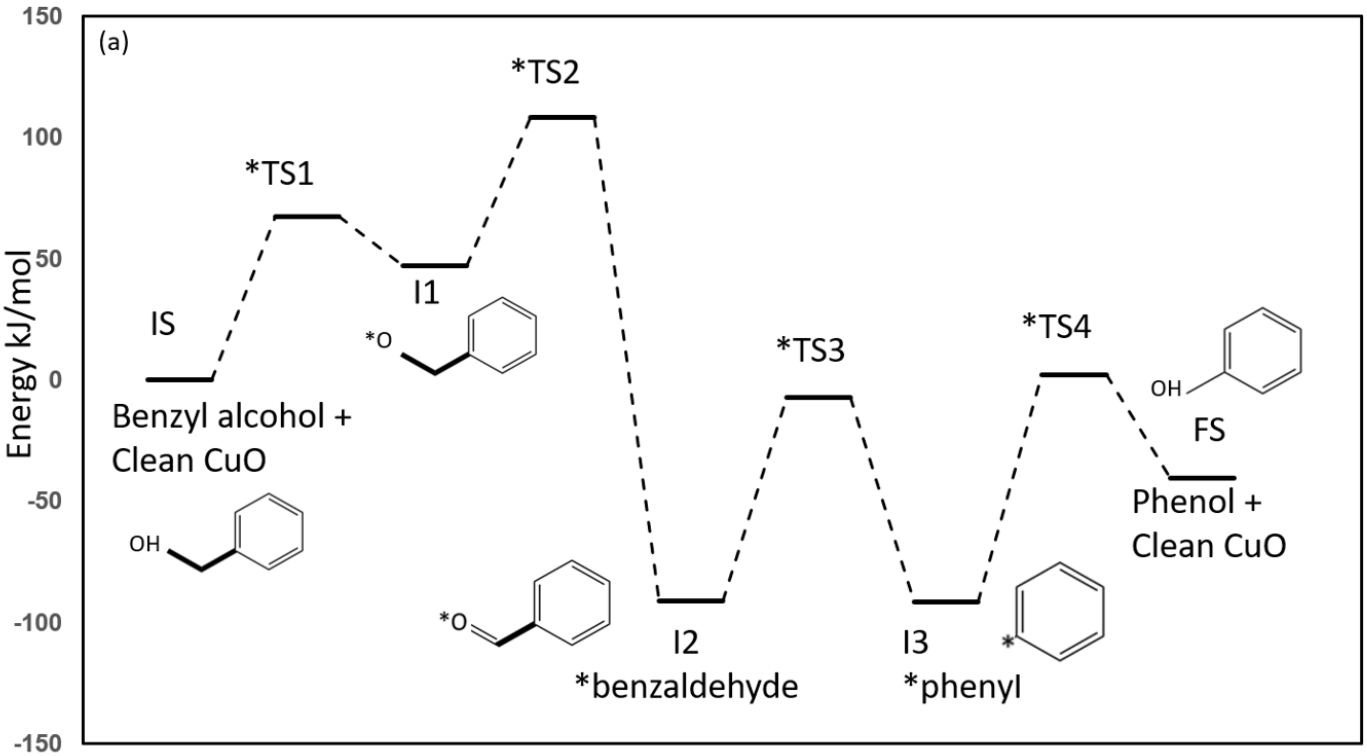

Figure 5. Free Energy profile for the catalytic conversion of benzyl alcohol to phenol on CuO (111) surface, via the most favored pathway indicated in Figure 4. Molecular structures of all reaction intermediates and transition states are provided in the supporting information (Figure. S11).

and S10). The most preferred reaction step after that is the activation of the C-H bond by surface adsorbed OH group to form adsorbed benzaldehyde, with the activation barrier of 61 kJ/mol. In this reaction step, surface adsorbed OH group assisted C-H activation is preferred over the C-H activation via surface lattice oxygen. This suggests that the surface adsorbed OH group could enhance reaction kinetics, confirming the experimental hypothesis. It is also important to mention that the reaction free energy of this step is -138 kJ/mol (compared to -71 kJ/mol for the C-H activation via surface lattice oxygen), thus revealing that benzaldehyde is strongly adsorbed on the catalyst surface. The DFT calculated free energy barrier for benzaldehyde desorption is over 200 kJ/mol, which further explains why benzaldehyde is not observed as a major product in the experiments though it is an intermediate in the reaction. Further, C-C cleavage between the aldehyde group and phenyl ring (the transition state is shown in **Figure S9**) was favoured kinetically over C-O and C-H activation (activation barriers are shown in Fig 4). The adsorbed phenyl group ($*C_6H_5$) on the catalyst surface would undergo hydroxylation to form phenol, a major product observed in the experiment (the transition state is shown in **Figure S9**)**.** The free energy barrier and reaction free energy for phenol formation are 93 and 51 kJ/mol, respectively. The free energy for phenol desorption from the catalyst surface was calculated to be only 21 kJ/mol. The DFT computed reaction pathway from benzyl alcohol to phenol (Fig. 5) is in agreement with the experimental results, as benzaldehyde is observed as an intermediate and OH group from water plays a direct role in the formation of phenol. The source of the surface OH group and the importance of benzaldehyde as an intermediate in the reaction pathway would be discussed further in the following sections.

The role of water/hydrogen peroxide in the formation of phenol. The most favored first activation of benzyl alcohol, as shown by DFT calculations, results in the dissociation of the OH group of the alcohol. Additionally, water is suggested to be the source of the surface OH group, via high-frequency ultrasound-induced dissociation. The activation energy barrier and reaction free energy for water dissociation on CuO (111) are 218 kJ/mol (significantly lower than C-O dissociation barrier of benzyl alcohol to generate OH species on the catalyst surface) and -30kJ/mol, respectively. The high reaction barrier indicates that without high-frequency ultrasound, it is unlikely for water to dissociate on the catalyst surface at 25 ºC. The negative reaction free energy shows that the reaction is thermodynamically feasible. Also, it is significantly lower than the non-catalytic dissociation energy of water, 492kJ/mol[57], suggesting that the presence of CuO would promote water dissociation on its surface to form adsorbed H and OH groups (**Figure S10**). Since the oxygen in the hydroxyl group of the reactant benzyl alcohol remains attached to the dissociated –CHO group (in the DFT computed minimum energy pathway), the OH hydroxylating the phenyl ring to form phenol (in the final step of the pathway shown in **Figure 5**) has to originate from water. This is in agreement with the isotope labelling experiments that demonstrated the incorporation of OD from D_2O into phenol. Hence, it can be conclusively said that in addition to catalyzing C-H activation, OH from water also incorporated itself into the aromatic ring after the C-C cleavage of benzaldehyde to form phenol.–H_2O_2 can also generate OH groups adsorbed on the CuO surface by dissociating into two OH fragments, catalyzed by CuO.[45] The free energy of the formation of adsorbed OH species from hydrogen peroxide on CuO(111) is −28 kJ/mol and the activation barrier is only 22 kJ/mol, suggesting the kinetic feasibility of the dissociation of H_2O_2 even without ultrasound irradiation. Hence, reactions performed in the presence of H_2O_2 under silent conditions at 62°C resulted in the formation of phenol (~16% yield) at a benzyl alcohol conversion of ~35% within 2h of reaction irradiation time (**Table S3, entry 3**) and remained constant even up to 6 h due to the depletion of H_2O_2.The reaction free energies of dissociation of H_2O and H_2O_2 on the catalyst surface indicate that the adsorption of the OH group on the catalyst surface is highly exergonic and stable, which further confirms the experimental observation that the presence of CuO suppresses OH recombination (**Figure 3(e)**) as OH would tend to be adsorbed on the catalyst surface.

Benzaldehyde and hydroxy-benzyl alcohol reactions. Benzaldehyde and benzoic acid are often considered major products of benzyl alcohol oxidation [14, 17, 58]. However, a low yield (< 3 %) of benzaldehyde and no benzoic acid was observed in this work. Benzaldehyde is shown as a key intermediate species and phenol was still the major product with benzaldehyde as the reactant. An alternative pathway suggested for benzaldehyde is to form benzoic acid, as shown in **Figure 4**. DFT computations were performed to investigate the pathway to phenol, via benzaldehyde oxidation to benzoic acid, followed by C-C cleavage between the acid group and the phenyl ring. The C-H activation barrier for benzaldehyde via

surface O is 93kJ/mol, followed by OH addition with the free energy barrier of 113 kJ/mol, to form benzoic acid (**Figure 4**). Since these activation barriers are higher than the C-C cleavage pathway from benzaldehyde, it is unlikely for benzoic acid to be a reaction intermediate. However, if benzoic acid is the reactant, it would also convert to phenol via C-C cleavage on CuO (as observed in the experiments), with the free energy barrier of 96 kJ/mol, followed by the hydroxylation step, as shown before. The reason that C-C cleavage is more facile for both benzaldehyde and benzoic acid is that the aromatic ring is not able to interact strongly enough with the metal oxide surface, and adsorption occurs via the aldehyde and acid groups. With *para*-hydroxy-benzyl alcohol as the reactant, *para*-hydroxy-benzaldehyde and hydroquinone were observed as products in the experiments. This also suggests that hydroxy-benzyl alcohol goes through the same activation pathway as benzyl alcohol, irrespective of the additional OH group present on the aromatic ring. The adsorption configuration of *para*-hydroxy-benzyl alcohol on CuO (111) was investigated and the most stable adsorption configuration (**Figure S11**) was similar to the adsorption configuration for benzyl alcohol, via the alcohol group. The OH group on the aromatic ring does not interact with the catalyst surface and hence it would not affect the reaction mechanism.

Conclusions

In summary, using a synergistic combination of ultrasound and earth-abundant metal oxide catalysis, we demonstrated a novel approach to demethylenate benzyl alcohol to phenol, at room temperature and using water as a solvent. The reaction mechanism involves the sequential activation of OH and C-H bonds in benzyl alcohol to form adsorbed benzaldehyde as an intermediate, which further undergoes C-C cleavage to form the phenyl ring. The phenyl ring is then hydroxylated to form phenol. Unlike typical condensed phase catalytic chemistry where water is either believed to be just a solvation medium and or may play an indirect role in the chemistry by altering reaction kinetics and thermodynamics, we reveal that ultrasound induces water dissociation and the copper oxide catalyst stabilizes the dissociated OH groups via adsorption. The adsorbed OH group plays a dual role; it activates the strong C-H bond in the reaction pathway and later gets incorporated into the phenyl ring during its hydroxylation. We also demonstrated that the reaction mechanism remains unchanged for para hydroxyl-benzyl alcohol, producing hydroquinone. Perspectively, these results demonstrate that a switch from a batch ultrasound sonolysis to a continuous flow sono-reactor, along with its coupling with a catalytic strategy will offer promising approaches and a technological breakthrough for the efficient intensification and productivity enhancement of chemicals synthesis.

Acknowledgement

T.B, F.J and PNA are grateful to the CNRS, the University of Poitiers, and the Region Nouvelle Aquitaine. The ANR JCJC AminoSound Project ID ANR-20-CE07-0006 is acknowledged for financial support. SHM and SJ acknowledge the financial support from Natural Sciences and Engineering Research Council (NSERC) Canada via its Discovery Grants program and the University of Alberta. Computational support was provided by the Digital Research Alliance of Canada (alliancecan.ca).

Conflicts of interest

There are no conflicts to declare.

References

1. T. J. Mason, *Advances in sonochemistry*, Elsevier, 1996.
2. K. S. Suslick, D. A. Hammerton and R. E. Cline, *Journal of the American Chemical Society*, 1986, **108**, 5641-5642.
3. K. S. Suslick, *Scientific American*, 1989, **260**, 80-87.
4. E. A. Neppiras, *Physics reports*, 1980, **61**, 159-251.
5. P. N. Amaniampong, Q. T. Trinh, K. de Oliveira Vigier, D. Q. Dao, N. H. Tran, Y. Wang, M. P. Sherburne and F. o. Jérôme, *Journal of the American Chemical Society*, 2019, **141**, 14772-14779.
6. S. K. Bhangu, G. Bocchinfuso, M. Ashokkumar and F. Cavalieri, *Nanoscale Horizons*, 2020, **5**, 553-563.
7. I. D. Manariotis, H. K. Karapanagioti and C. V. Chrysikopoulos, *Water Research*, 2011, **45**, 2587-2594.
8. P. Juliano, F. Bainczyk, P. Swiergon, M. I. M. Supriyatna, C. Guillaume, L. Ravetti, P. Canamasas, G. Cravotto and X.-Q. Xu, *Ultrasonics sonochemistry*, 2017, **38**, 104-114.
9. P. N. Amaniampong, A. Karam, Q. T. Trinh, K. Xu, H. Hirao, F. Jérôme and G. Chatel, *Scientific reports*, 2017, **7**, 1-8.
10. P. N. Amaniampong, J. L. Clément, D. Gigmes, C. Ortiz Mellet, J. M. Garcia Fernandez, Y. Blériot, G. Chatel, K. De Oliveira Vigier and F. Jérôme, *ChemSusChem*, 2018, **11**, 2673-2676.
11. P. N. Amaniampong and F. Jérôme, *Current opinion in green and sustainable chemistry*, 2020, **22**, 7-12.
12. H. Mei, Z. Gao, K. Zhao, M. Li, M. Ashokkumar, A. Song, J. Cui, F. Caruso and J. Hao, *Angewandte Chemie*, 2021, **133**, 21699-21705.

13. A. Humblot, L. Grimaud, A. Allavena, P. N. Amaniampong, K. de Oliveira Vigier, T. Chave, S. Streiff and F. Jerome, *Angewandte Chemie*, 2021, **133**, 25434-25438.
14. H. Li, F. Qin, Z. Yang, X. Cui, J. Wang and L. Zhang, *Journal of the American Chemical Society*, 2017, **139**, 3513-3521.
15. K. R. Seddon and A. Stark, *Green chemistry*, 2002, **4**, 119-123.
16. A. K. Vannucci, J. F. Hull, Z. Chen, R. A. Binstead, J. J. Concepcion and T. J. Meyer, *Journal of the American Chemical Society*, 2012, **134**, 3972-3975.
17. L. G. Marinescu and M. Bols, *Angewandte Chemie*, 2006, **118**, 4706-4709.
18. K. Amakawa, Y. V. Kolen'ko, A. Villa, M. E. Schuster, L.-I. Csepei, G. Weinberg, S. Wrabetz, R. Naumann d'Alnoncourt, F. Girgsdies, L. Prati, R. Schlögl and A. Trunschke, *ACS Catalysis*, 2013, **3**, 1103-1113.
19. J. Long, X. Xie, J. Xu, Q. Gu, L. Chen and X. Wang, *ACS Catalysis*, 2012, **2**, 622-631.
20. J. Fan, Y. Dai, Y. Li, N. Zheng, J. Guo, X. Yan and G. D. Stucky, *Journal of the American Chemical Society*, 2009, **131**, 15568-15569.
21. R. J. Schmidt, *Applied Catalysis A: General*, 2005, **280**, 89-103.
22. V. Zakoshansky, *Petroleum Chemistry*, 2007, **47**, 273-284.
23. P. N. Amaniampong, Q. T. Trinh, K. De Oliveira Vigier, D. Q. Dao, N. H. Tran, Y. Wang, M. P. Sherburne and F. Jérôme, *Journal of the American Chemical Society*, 2019, **141**, 14772-14779.
24. S. Koda, T. Kimura, T. Kondo and H. Mitome, *Ultrasonics Sonochemistry*, 2003, **10**, 149-156.
25. J. J. Kwan, G. Lajoinie, N. de Jong, E. Stride, M. Versluis and C. C. Coussios, *Physical Review Applied*, 2016, **6**.
26. J. J. Kwan, R. Myers, C. M. Coviello, S. M. Graham, A. R. Shah, E. Stride, R. C. Carlisle and C. C. Coussios, *Small*, 2015, **11**, 5305-5314.
27. X. Su, R. G. Thomas, L. D. Bharatula and J. J. Kwan, *Sci Rep*, 2019, **9**, 9612.
28. U. S. Jonnalagadda, T. M. Nguyen, F. Li, J. H. C. Lee, X. Liu, A. Goto and J. J. Kwan, *Macromolecular Chemistry and Physics*, 2020, **221**.
29. X. Su, U. S. Jonnalagadda, L. D. Bharatula and J. J. Kwan, *Ultrasonics Sonochemistry*, 2021, **79**.
30. G. Kresse and J. Furthmüller, *Computational Materials Science*, 1996, **6**, 15-50.
31. G. Kresse and J. Hafner, *Physical Review B*, 1993, **47**, 558-561.
32. G. Kresse and J. Furthmüller, *Physical Review B*, 1996, **54**, 11169-11186.
33. G. Kresse and J. Hafner, *Journal of Physics: Condensed Matter*, 1994, **6**, 8245-8257.
34. P. E. Blöchl, *Physical Review B*, 1994, **50**, 17953-17979.
35. G. Kresse and D. Joubert, *Physical Review B*, 1999, **59**, 1758-1775.
36. J. P. Perdew, K. Burke and M. Ernzerhof, *Physical Review Letters*, 1996, **77**, 3865-3868.
37. J. Klimeš, A. Bowler Dr Fau - Michaelides and A. Michaelides, 2010.
38. J. Klimeš, D. R. Bowler and A. Michaelides, *Physical Review B*, 2011, **83**, 195131.
39. K. Bhola, J. J. Varghese, L. Dapeng, Y. Liu and S. H. Mushrif, *The Journal of Physical Chemistry C*, 2017, **121**, 21343-21353.
40. P. N. Amaniampong, Q. T. Trinh, J. J. Varghese, R. Behling, S. Valange, S. H. Mushrif and F. Jérôme, *Green Chemistry*, 2018, **20**, 2730-2741.
41. G. Henkelman and H. Jónsson, *The Journal of Chemical Physics*, 2000, **113**, 9978-9985.
42. H. Jónsson, G. Mills and K. W. Jacobsen, 1998.
43. G. Henkelman, B. P. Uberuaga and H. Jónsson, *The Journal of Chemical Physics*, 2000, **113**, 9901-9904.
44. D. Sheppard, R. Terrell and G. Henkelman, *The Journal of Chemical Physics*, 2008, **128**, 134106.
45. P. N. Amaniampong, Q. T. Trinh, B. Wang, A. Borgna, Y. Yang and S. H. Mushrif, *Angewandte Chemie*, 2015, **127**, 9056-9061.
46. Malcolm W. Chase, Jr., *NIST-JANAF thermochemical tables*, Fourth edition. Washington, DC : American Chemical Society ; New York : American Institute of Physics for the National Institute of Standards and Technology, 1998., 1998.
47. C. Gong and D. P. Hart, *The Journal of the Acoustical Society of America*, 1998, **104**, 2675-2682.
48. J. J. Kwan, R. Myers, C. M. Coviello, S. M. Graham, A. R. Shah, E. Stride, R. C. Carlisle and C. C. Coussios, *small*, 2015, **11**, 5305-5314.
49. X. Su, R. G. Thomas, L. D. Bharatula and J. J. Kwan, *Scientific reports*, 2019, **9**, 1-13.
50. U. Jonnalagadda, X. Su and J. Kwan, *Ultrasonics sonochemistry*, 2021, **73**, 105530.
51. C. D. Arvanitis, M. Bazan-Peregrino, B. Rifai, L. W. Seymour and C. C. Coussios, *Ultrasound in medicine & biology*, 2011, **37**, 1838-1852.
52. J. Kwan, G. Lajoinie, N. de Jong, E. Stride, M. Versluis and C. Coussios, *Physical review applied*, 2016, **6**, 044004.
53. R. G. Thomas, U. S. Jonnalagadda and J. J. Kwan, *Langmuir*, 2019, **35**, 10106-10115.
54. S. Haouache, A. Karam, T. Chave, J. Clarhaut, P. N. Amaniampong, J. M. G. Fernandez, K. D. O. Vigier, I. Capron and F. Jérôme, *Chemical science*, 2020, **11**, 2664-2669.
55. T. Leighton, M. Pickworth, A. Walton and P. Dendy, *Physics in Medicine & Biology*, 1988, **33**, 1239.
56. Y. T. Didenko, D. Nastich, S. Pugach, Y. Polovinka and V. Kvochka, *Ultrasonics*, 1994, **32**, 71-76.
57. O. V. Boyarkin, M. A. Koshelev, O. Aseev, P. Maksyutenko, T. R. Rizzo, N. F. Zobov, L. Lodi, J. Tennyson and O. L. Polyansky, *Chemical Physics Letters*, 2013, **568-569**, 14-20.
58. C. M. Crombie, R. J. Lewis, R. L. Taylor, D. J. Morgan, T. E. Davies, A. Folli, D. M. Murphy, J. K. Edwards, J. Qi and H. Jiang, *ACS Catalysis*, 2021, **11**, 2701-2714.